# Yb:YAG master oscillator power amplifier for remote wind sensing

A. K. Sridharan,* S. Saraf, and R. L. Byer

Ginzton Laboratory, Stanford University, Stanford, California 94305, USA

*Corresponding author: s.arun.kumar@stanfordalumni.org

Received 26 April 2007; revised 27 July 2007; accepted 29 July 2007;
posted 31 July 2007 (Doc. ID 82446); published 18 October 2007

We have demonstrated key advances towards a solid-state laser amplifier at 1.03 μm for global remote wind sensing. We designed end-pumped zig-zag slab amplifiers to achieve high gain. We overcame parasitic oscillation limitations using claddings on the slab's total internal reflection (TIR) and edge surfaces to confine the pump and signal light by TIR and allow leakage of amplified spontaneous emission rays that do not meet the TIR condition. This enables $e^3$, $e^5$, and $e^8$ single-, double-, and quadruple-pass small-signal amplifier gain, respectively. The stored energy density is 15.6 J/cm$^3$, a record for a laser-diode end-pumped Yb:YAG zig-zag slab amplifier. © 2007 Optical Society of America

*OCIS codes:* 140.0140, 140.3280, 140.3480, 140.3538, 140.3580, 140.3615.

## 1. Introduction

Space-based tropospheric wind velocity measurements require high-pulse-energy laser sources with a high degree of spectral and spatial coherence. A coherent Doppler wind light detection and ranging (lidar) system requires an efficient, narrow linewidth ($< 1.3$ MHz), eye-safe (i.e., $\lambda > 1.4$ μm) laser source that generates pulses with energies exceeding 150 mJ at 40 Hz [1]. In the eye-safe near-IR wavelengths, Tm:Ho:YAG flashlamp pumped lasers were first developed in 1990 by Henderson and co-workers at Coherent Technologies [2]. This was followed by a diode-pumped 2.02 μm Tm:YAG laser in 1991 [3] and was implemented in a wind-lidar system in 1993 [4,5]. *Q*-switched, single-frequency, 2 μm sources developed at NASA's Langley Research Center over the past decade now operate at the 1 J level at 5% optical efficiency [6].

In recent years, there has also been considerable interest in demonstrating a lidar system in the eye-safe 1.55 μm wavelength region. Operating at 1.55 μm has several advantages compared to 2 μm operation. The laser transmitter has reduced energy requirements because the aerosol backscatter coefficient is proportional to $\lambda^{-1} - \lambda^{-2}$ [7]. The relatively fewer molecular absorption lines in this band compared to the 2 μm range gives greater flexibility to the laser engineer. Shorter wavelength operation allows for a smaller velocity resolution ($\Delta v$) and range resolution ($\Delta r$) product given by $\Delta v \Delta r = c\lambda/3.4\pi$ [8]. Operating in the telecommunications band also allows dovetailing of many commercial products to achieve lower costs. For example, the use of fibers and fiber couplers, master oscillators, preamplifiers, isolators, and detectors is possible [9].

The two traditional approaches, namely, *Q*-switched oscillators at 1.55 μm and 1 μm pumped 1.55 μm optical parametric oscillators, are either inefficient or difficult to operate with the required linewidth [1]. To meet the remote wind-sensing requirements, we have designed and demonstrated key elements of a high-pulse-energy, 1.03 μm, laser amplifier system designed to generate 1 J/μs pulses. To generate eye-safe radiation, the 1 μm source can be used to pump a parametric amplifier for downconversion to a 1.55 μm, narrow linewidth, output [1].

*Q*-switched oscillators and the master oscillator power amplfier (MOPA) form the two main approaches to meeting the laser requirements at 1.03 μm. Traditional *Q*-switched oscillators produce very short pulses of less than 10 ns duration and have linewidths much greater 1 MHz. They are therefore not suitable for coherent wind velocity measurements that rely on aerosol backscatter. Schemes for gener-

0003-6935/07/307552-14$15.00/0

ating longer $Q$-switched pulses have been studied [10–16]. Depending on the approach, the lasers are either inefficient due to prelasing, postlasing, and the loss required to maintain a good pulse shape or have pulse-to-pulse jitter and require complicated switching electronics.

The MOPA configuration provides the ability to tailor the pulse width, beam divergence, and spectral width of the output pulses with low power components prior to power amplification. Pulse energy scaling is achieved by cascading power amplifiers. Furthermore, with this approach the laser can operate with longer pulse lengths, achieve good coherence control, better power and timing stability, and operational reliability. For example, single-element failure in the amplifier chain reduces output power and is not catastrophic when compared to a conventional $Q$-switched laser.

In this paper, we discuss the design, modeling, fabrication, and testing of an end-pumped slab preamplifier that can be incorporated in a MOPA system. We also present design calculations for the two-slab power amplifier that can generate output at 1 J in a 1 μs duration pulse. Although the efficiency of the MOPA system is determined by the efficiency of the power amplifier, a reliable high-gain preamplifier design is critical to achieving efficient energy extraction from the power amplifier.

Efficient energy storage and extraction are the key performance indicators of a pulsed MOPA system. The first goal of amplifier design is to maximize the storage efficiency. The second goal is to tailor the signal pulses in energy and duration to extract a significant fraction of the stored energy by stimulated emission. Meeting these objectives is especially important for a space-based operation where solar panels and batteries add significantly to the cost. The system is designed to achieve both these objectives. We discuss first the influence of these objectives on system design.

### A. Energy Storage

#### 1. *Definition*

The unsaturated gain of an optical amplifier, $G$, is given by $G = e^{g_0 l_{\text{eff}}}$, where $g_0$ ($\text{cm}^{-1}$) is the small signal gain coefficient and $l_{\text{eff}}$ is the signal's optical path length through the gain medium. The stored energy, $E_{\text{stored}}$, in this solid-state amplifier is given by [17]

$$E_{\text{stored}} = g_0 F_{\text{sat}} V, \tag{1}$$

where $F_{\text{sat}}$ ($\text{J/cm}^2$) is the gain medium saturation fluence, and $V$ ($\text{cm}^3$) is the amplifier's gain volume. The saturation fluence, a fundamental property of a laser gain medium, is given by [18]

$$F_{\text{sat}} = \frac{h\nu_e}{\sigma_{\text{dyn}}{}^e}, \tag{2}$$

where $h$ is Planck's constant, $\nu_e$ is the frequency of the amplified radiation, and $\sigma_{\text{dyn}}{}^e$ is the dynamic emission cross section given as $\sigma_{\text{dyn}}{}^e = \gamma_m \sigma_{is}{}^e$. $\gamma_m$ is a material parameter given by $\gamma_m = f_a{}^e + f_b{}^e$ that relates the reduction in inversion density for each stimulated or spontaneous emission event. $f_a{}^e$ and $f_b{}^e$ are defined in Subsection 1.A.3. $\sigma_{is}{}^e$ is the spectroscopic [state to state or inter-Stark (*is*)] emission cross section given by $\sigma_{is}{}^e = \sigma_{\text{eff}}{}^e / f_b{}^e$. The effective or intermanifold emission cross section is $\sigma_{\text{eff}}{}^e$ and is typically derived from spectroscopic measurements. The gain and saturation fluence must be maximized for efficient energy storage.

#### 2. *Limits to Stored Energy*

Single-pass amplification of spontaneous emission (SE) depletes the population inversion and is the fundamental limit to gain and stored energy [19–21]. Closed loop amplified spontaneous emission (ASE) paths that have more gain than loss form a parasitic oscillation mode, deplete the population inversion, and pin the gain below the ASE limit. For example, to our knowledge, the highest ASE-limited logarithmic gain in a pulsed 1.0641 μm Nd:YAG zig-zag slab amplifier is 4.6–5.3 [22]. Further, a parasitic-limited logarithmic gain of 7.53 has been achieved in a pulsed 1.047 μm Nd:YLF rod amplifier [23]. In both cases, the stored energy density is less than or equal to $0.5\ \text{J/cm}^3$ and operating at the highest gain levels comes at the expense of decreased energy storage efficiency due to ASE losses. The exact parasitic oscillation limited gain for a particular crystal depends on its physical and spectroscopic properties, geometry, and the surfaces' reflectivity and must be experimentally determined.

#### 3. *Choice of Gain Material*

In an amplifier with ASE or parasitic-oscillation-limited gain, the stored energy is maximized by choosing a material with the highest saturation fluence subject to the ability to extract the stored energy. Among the low emission cross-section materials that maximize the saturation fluence, Nd:glass [17,24–26] and Yb:YAG are most advanced. Yb:YAG, a material first discovered in the early, 1960's [27], has the lowest emission cross section, the highest emission saturation fluence, and the highest energy storage density [1]. An attractive feature of Yb:YAG is that it has one of the longest upper-state fluorescence lifetimes, $\tau$. $g_0 l_{\text{eff}} \propto P_{\text{pump}}{}^{pk} \tau$ [28] where $P_{\text{pump}}{}^{pk}$ is the peak incident pump power. Since the $\tau$ for Yb:YAG is three times higher than that of Nd:glass, a corresponding 1/3 fewer (or lower-power pump diodes) are required to achieve the same logarithmic gain or stored energy. This is important for space applications because of reduced size, power, and cost.

The quasi-three-level nature of Yb:YAG has implications for amplifier crystal design. The $Yb^{3+}$ ion has a $4f^{13}$ shell that has an electron missing compared to a filled shell [29]. This shell is located approximately 10,000 $\text{cm}^{-1}$ above the ground level. The crystal's internal electric field results in Stark splitting of the level by approximately 700 $\text{cm}^{-1}$ [30]. For an ensem-

ble of $Yb^{3+}$ ions in the YAG host crystal, the relative population density for each Stark-split level is given by the Boltzmann factor ($e^{-\Delta E/k_bT}$) where $k_b$ is Boltzmann's constant, $T$ is the crystal temperature, and $\Delta E$ is the energy of the Stark level relative to the lowest Stark-level within the manifold. $f_a^p$ is the Boltzmann occupation factor of the initial (lower manifold) Stark level coupled by the pump radiation at 940 nm. $f_b^p$ is the Boltzmann occupation factor of the final (upper manifold) Stark level coupled by the pump radiation. $f_a^e$ and $f_b^e$ are similarly defined for the signal radiation at 1030 nm.

In Yb:YAG, $f_a^e = 0.046$, which means that 4.6% of the dopant atoms are in the lower laser level at room temperature. As a consequence, a minimum pump intensity, $I_{\min}$, needs to be maintained throughout the doped region of the crystal to achieve a positive local inversion density and prevent reabsorption loss for the signal [18,29,31]. An optimal atomic percent doping and absorption-axis-length product needs to be chosen to maximize gain. Furthermore, efficient pump absorption requires a pump intensity in excess of the pump saturation intensity, which for the 941 nm transition in Yb:YAG is given as $I_{\text{sat}}^{\text{pump}} = h\nu_p/\sigma_{\text{dyn}}{}^p\tau = 24\ \text{kW/cm}^2$ where $\sigma_{\text{dyn}}{}^p = \sigma_{\text{eff}}{}^p[(f_a^p + f_b^p)/f_a^p]$ [18]. Commercial, high-peak-power, diode lasers available today enable pumping at intensities above the pump saturation intensity. As a result, there is bleaching of the laser crystal and the gain is limited by ASE and parasitic oscillations, and not by inadequate pump absorption.

The final advantageous feature of Yb:YAG concerns laser-amplifier efficiency. The energy storage efficiency is defined in terms of the Stokes efficiency and the pump quantum efficiency, $\eta_{NP}$ [31]. The Stokes efficiency is the ratio of signal and pump photon energies. For Yb:YAG this is 0.91, approximately 0.15 higher than most of the other materials that oscillate in the 1 μm band. We have chosen to operate with 3% Yb:YAG crystals in this work. At this doping level concentration quenching [32] and nonradiative decay [33] are not present.

## B. Energy Extraction

### 1. *General Considerations for Efficient Energy Extraction*

To achieve power scaling in the MOPA configuration, the preamplifiers must have high gain and the power amplifiers must be designed to allow efficient energy extraction. The output fluence of a solid-state power amplifier is given by the Franz–Nodvik relation [17,34] as

$$F_{\text{out}} = \eta_{\text{overlap}} F_{\text{sat}} \ln\{1 + [e^{F_{\text{in}}/F_{\text{sat}}} - 1]e^{g_0 l_{\text{eff}}}\}, \quad (3)$$

where $F_{\text{out}}$ is the output fluence, $F_{\text{in}}$ is the input signal fluence, $g_0$ is the small signal gain coefficient, $l_{\text{eff}}$ is the signal optical path length, and $F_{\text{sat}}$ is the saturation fluence of the gain medium. The extraction efficiency $\eta$ for the amplifier is defined as

$$\eta = \eta_{\text{overlap}} \frac{F_{\text{out}} - F_{\text{in}}}{F_{\text{sat}} g_0 l_{\text{eff}}}, \quad (4)$$

where $\eta_{\text{overlap}}$ is the spatial mode-overlap efficiency factor. For $\eta_{\text{overlap}} = 1$ and $g_0 l_{\text{eff}} = 3$, $F_{\text{in}} > 0.4F_{\text{sat}}$ is needed to extract greater than 93% of the stored energy from the double-passed power amplifier. In practice, reduced mode overlap reduces the extraction efficiency significantly below the theoretical limit of 100%.

### 2. *Choice of Signal Pulse Width*

In addition to the pump and signal mode overlap, extraction efficiency is limited by the onset of optical damage. The optical surface damage fluence, $F_{\text{dam}}$, is a function of the signal pulse width, $\Delta t$. For $\Delta t > \approx 100$ ps, the heat deposited causes a temperature rise that is limited by conduction and diffusion into the lattice. At a particular critical temperature, optical damage is caused by fracture, melting or boiling. Wood [35] shows that the time needed to reach the critical temperature scales as $\sqrt{\Delta t}$ and that the damage fluence is given by

$$F_{\text{dam}}(\Delta t) = F_{\text{dam}}(\Delta t_{\text{ref}})\sqrt{\frac{\Delta t}{\Delta t_{\text{ref}}}}, \quad (5)$$

where $\Delta t$ is the signal pulse duration, and $F_{\text{dam}}(\Delta t_{\text{ref}})$ is the signal damage fluence for pulses greater than 100 ps in duration (i.e., $\Delta t_{\text{ref}} > 100$ ps). Figure 1 shows a plot of Eq. (5), which illustrates the damage fluence's dependence on pulse duration for YAG. The damage fluence for 10 ns duration pulses is approximately 10 $\text{J/cm}^2$. The optical fluence damage threshold increases by the square root of the pulse length and thus is greater than 100 $\text{J/cm}^2$ for 1 μs pulses in YAG. At 1.03 μm, the Yb:YAG emission saturation fluence at room temperature is 8.66 $\text{J/cm}^2$ (assuming $f_b^e = 0.772$ and $\sigma_{\text{eff}}{}^e = 2.1 \times 10^{-20}\ \text{cm}^2$ [18]). With 10 ns duration pulses, it is not possible to saturate this amplifier and extract efficiently without optical

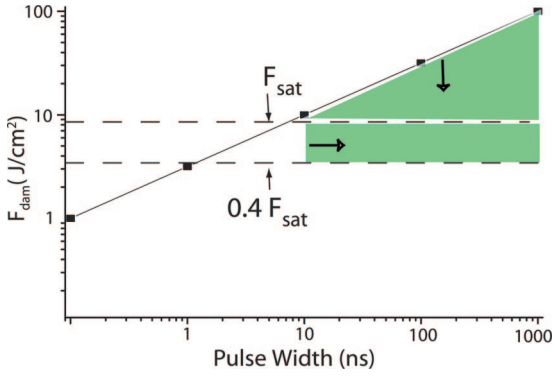


Fig. 1. (Color online) Damage fluence limit in Yb:YAG $\text{J/cm}^2$ versus pulse width (ns). Operating with input and output fluences in the shaded region enables efficient energy extraction without optical damage.

damage. Operation with 1 μs signal pulses allow input fluences that exceed the saturation fluence for efficient extraction while staying below the damage fluence limit as shown by the shaded region in Fig. 1.

### 3. *Slab Laser Architecture*

Future space-based wind-sensing missions may well require lasers that exceed current power expectations and operate at higher pulse energies, repetition rates, and higher output power. In addition to scaling in average power, remote wind sensing requires a laser architecture that enables pulse energy scaling. Suppression of parasitic oscillations is required for efficient energy storage and extraction. For example, tapered diameter rods with flanged endcaps have been explored at Lawrence Livermore National Laboratory (LLNL) to suppress parasitic oscillations in Yb:YAG rods [36].

We chose to pursue an alternative laser architecture based on slab because of their advantageous properties. Slabs were invented at General Electric in 1972 [37] and further developed there during the 1970s and 1980s [38,39]. They have also been extensively studied in the Byer [22,40–47], Northrup Grumman Space Technology (NGST) [48–51], LLNL [52,53], University of Rochester [54], Berlin [55–57], and Bass [58–61] groups, among others. Thin disk lasers, a form of slab lasers, have been extensively developed by Giesen's group [62–64] and have reached the 1 kW class in multiple transverse modes [65]. Thin disk lasers require a complicated optomechanical design due to the multiple passes of pump light for efficient absorption. Energy storage and extraction with good beam quality is challenging because of the short gain length, transverse ASE, and one-sided cooling. The zig-zag, rectilinear geometry, slab-based MOPA system can scale to higher stored energy while maintaining a high beam quality. The slab lasers are cooled symmetrically on both sides and their average power output scales with the cooled area.

The comparative advantages of zig-zag, rectilinear geometry slabs as compared to rods are also well-known [41]. In a traditional face-pumped slab [43], there is a 1-D thermal gradient and the zig-zag optical path averages out the associated first-order thermal lens [40,42]. Depolarization is minimized in slabs because, to first order, there is a 1-D stress induced polarization that is coaligned with the input beam polarization. The stress fracture limit of a slab scales as the average power, which in turn scales as the cooled area of the slab.

Early zig-zag, rectilinear geometry slab laser designs had low efficiencies due to flashlamp pumping. Residual phase distortions and a complex direct water-cooled laser head added to the engineering challenges [40]. Most of these engineering problems have now been solved by laser diode pumping through the end [50] and edge [44] of conduction-cooled zig-zag slabs [46]. Nd:YAG zig-zag end-pumped slab lasers now operate at multikilowatt output powers with excellent beam quality [51]. Edge-pumped designs scale well at very high average powers because the cooled area can be increased while simultaneously increasing pump absorption and preventing stress fracture [47].

We are interested in a compact and efficient conduction-cooled laser architecture for space-based remote sensing. Specifically, our goal is to design a 1 J/μs, 40 Hz, slab-based MOPA system with 40 W of average output power. Slab amplifiers operating at this power level have been implemented in the edge-, face-, and end-pumped configurations. The end-pumped designs are most efficient at low average powers. The slab cross-section area can be kept small and the length increased to achieve complete pump absorption. Further, unlike edge-pumped slabs, end-pumped slabs have edges whose reflectivity can be tailored to suppress parasitic oscillations. High-gains through enhanced parasitic suppression in Yb:YAG slabs form the key experimental achievements described in this paper. In Section 2 we discuss the end-pumped slab design and model the performance of the Yb:YAG slab amplifier.

## 2. End-Pumped Zig-Zag Slab Amplifier: Theory, Design, Modeling

The end-pumped Yb:YAG zig-zag slab amplifier is pumped by fiber-coupled laser diodes, re-imaged with a lens onto the end of the slab. The slab consists of a doped region bonded to undoped end caps [66] by a "chemically activated direct bonding" method [67]. The pump light refracts at the slanted end face and is confined by total internal reflection (TIR) on the four surfaces of the undoped end caps and is absorbed along the length of the doped region. The pump and signal are coupled into the slab from opposite ends for ease of alignment.

Figure 2 shows that the signal light is incident at an off-normal angle to the end face, propagates in the $x$–$z$ plane, and is confined in the slab via TIRs on the top-and-bottom (side) faces. The analytical relations that describe the performance of an end-pumped slab amplifier are introduced in this section and are used to design and model a slab preamplifier operated in the exponential gain (unsaturated) regime. The experimental performance is described in Section 3.

### A. Theory

Zig-zag slab laser design has been treated earlier by Eggleston *et al.* [41] and Kane *et al.* [42] and recently by Chen *et al.* [59,60]. Eggleston *et al.* [48] also extended the Franz–Nodvik amplifier analysis [34] to zig-zag slabs that had regions with and without standing waves.

Figure 2 also shows the geometry of a partially filled zig-zag slab in a section of the amplifier slab with regions that do and do not have power extracted by the incident optical beam. This beam overlap will be considered in our model. Using the Franz–Nodvik equations [34] and modifying the treatment of Eggelston *et al.* [48] to take into account the less than 100% fill factor in the transverse dimension, $E_{\text{out}}$ of the zig-zag end-pumped slab single-pass amplifier is given by

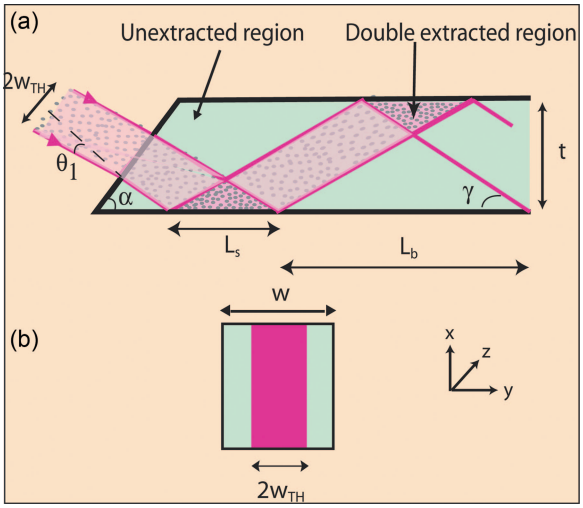


Fig. 2. (Color online) (a) Geometry of the partially filled slab at near normal incidence for a single-pass slab amplifier. The bounce period is $L_b$ and the overlap region has a length $L_s$. The distance between the two parallel lines that indicate the beam path represent the diameter of the Gaussian beam's top-hat equivalent. In reality, the tails of the Gaussian beam profile extend to the slab's edges. $w_g$ is chosen such that clipping losses are less than 2%. (b) The active cross section of the slab has a width of $2w_{TH}$ and a thickness of $t$. The active area is partially filled with incident signal power. The slab's cross-section area is given as $A_{\text{slab}} = w \times t$.

$$E_{\text{out}} = \eta_{s-\text{loss}} F_{\text{sat}} A_{\text{active}} \cos(\gamma) f(2-f) \times \ln\left[1 + \left(e^{E_{\text{in}}/F_{\text{sat}}A_{\text{active}}\cos(\gamma)f(2-f)} - 1\right)e^{g_0 l_{\text{eff}}}\right]. \quad (6)$$

In the small-signal gain limit (i.e., $E_{\text{in}}/A_{\text{active}} \cos(\gamma) f(2-f) F_{\text{sat}} \ll 1$ and also $E_{\text{in}} e^{g_0 l_{\text{eff}}}/A_{\text{active}} \cos(\gamma) f(2-f) F_{\text{sat}} \ll 1$), Eq. (6) reduces to

$$E_{\text{out}} = \eta_{s-\text{loss}} E_{\text{in}} e^{g_0 l_{\text{eff}}}, \quad (7)$$

where $\eta_{s-\text{loss}}$ is the single-pass optical transmission efficiency due to passive losses (i.e., scattering or diffraction) in the crystal. $E_{\text{in}}$ is the input signal energy, and $A_{\text{active}}$ is the active cross sectional area of the zig-zag slab that is probed by the incident beam and is equal to $2w_{TH}t$. Here $w_{TH}$ is the top-hat equivalent of the $\text{TEM}_{00}$ Gaussian beam $1/e^2$ radius in the slab and is defined by [68]

$$w_{TH} = w_g/\sqrt{2}, \quad (8)$$

and $t$ is the slab thickness. The propagation length of the signal beam inside the doped region is $l_{\text{eff}} = l_{\text{doped}}/\cos\gamma$ where $l_{\text{doped}}$ is the length of the doped region and $\gamma$ is the complementary angle to the angle of incidence at the TIR surface as shown in Fig. 2. The overlap factor $f$ for near normal incidence in a zig-zag slab can be calculated as

$$f = \frac{L_s}{L_b} = \frac{1}{\sqrt{2}} \frac{w_g}{t} \sec(\gamma), \quad (9)$$

where, $L_s$, is the overlap length given by

$$L_s = \sqrt{2}\,\frac{w_g}{\sin\gamma}, \quad (10)$$

and, $L_b$, is the bounce length given by

$$L_b = \frac{2t}{\tan\gamma}. \quad (11)$$

The logarithmic gain [18] is given by

$$g_0 l_{\text{eff}} = \Delta N(t) \sigma_{\text{dyn}}{}^e l_{\text{eff}}, \quad (12)$$

$$= \Delta N(t) \sigma_{\text{dyn}}{}^e \frac{l_{\text{doped}}}{\cos\gamma}, \quad (13)$$

$$= (N_u(t) - N_l(t)) \frac{\sigma_{\text{dyn}}{}^e}{\cos\gamma}, \quad (14)$$

where $\Delta N(t)$ is the population inversion density referenced to the Stark levels. $N_u(t)$ is the length-integrated upper laser level population density, and $N_l(t)$ is the length-integrated lower laser level population density. $N_u(t) = f_b{}^e * N_2(t)$, where $N_2(t)$ is the length-integrated excited manifold density given by Beach [69] as

$$N_2(t) = \int_{z=0}^{z=l_{\text{doped}}} n_2(z, t)\,dz, \quad (15)$$

where $n_2(z, t)$ is the excited manifold density, and $z$ is the propagation direction.

$N_2(t)$ is calculated by numerically integrating the differential equation given by [69]

$$\frac{dN_2(t)}{dt} = -\frac{\eta_{p-\text{loss}} I_{\text{in}}(t)}{h\nu_p}\left(e^{\sigma_{is}{}^p N_2{}^*(t)} - 1\right)\left(R_p e^{\sigma_{is}{}^p N_2{}^*(t)} + 1\right) - \frac{N_2(t)}{\tau}. \quad (16)$$

In this expression, $h$ is Planck's constant, $\nu_p$ is the pump excitation frequency, $\sigma_{is}{}^p$ is the spectroscopic [state to state or inter-Stark ($is$)] pump absorption cross section given as $\sigma_{is}{}^p = \sigma_{\text{eff}}{}^p/f_a{}^p$. The effective or intermanifold pump absorption cross section is $\sigma_{\text{eff}}{}^p$ and is typically derived from spectroscopic measurements [1]. $\tau$ is the excited state manifold's fluorescence lifetime, $R_p$ is the pump reflectivity (ranges from 0 to 1) at the slab's right end, and $N_2{}^*(t)$ is defined as

$$N_2{}^*(t) = (f_a{}^p + f_b{}^p) N_2(t) - f_a{}^p n_0 l_{\text{doped}}, \quad (17)$$

where $n_0$ is the combined density of the upper and lower manifolds. $I_{\text{in}}(t)$ is the peak incident pump in-

tensity at the amplifier crystal's input face given by

$$I_{\text{in}}(t) = \frac{P_{\text{pump}}^{pk}(t)}{A_{\text{beam}}^{\text{pump}}}, \tag{18}$$

where $P_{\text{pump}}^{pk}(t)$ is the peak incident pump power at the input face and $A_{\text{beam}}^{\text{pump}}$ is the focused spot size of the pump beam at the input face. Because of the large divergence angle (e.g., commercially available fiber-coupled diode lasers with 600 μm core diameter had an NA = 0.22 in 2002) of the focused pump light, the slab confines the pump light and $A_{\text{beam}}^{\text{pump}}$ is equal to $A_{\text{slab}} = w \times t$. The fraction of incident pump power that reaches the beginning of the doped region of the crystal, $\eta_{p-\text{loss}}$, is less than 1 because of the imperfect antireflection (AR) coating at the input end face, and less than 100% confinement due to TIR at the slab's side and edge faces.

The stored energy in the end-pumped, composite, slab amplifier is given by

$$E_{\text{stored}} = g_0 F_{\text{sat}} w t l_{\text{doped}}, \tag{19}$$

$$= g_0 F_{\text{sat}} w t l_{\text{eff}} \cos \gamma. \tag{20}$$

To model the power extraction from a power amplifier, the available power in the active cross section of this slab power amplifier is given by

$$E_{\text{avail}} = E_{\text{stored}} \frac{A_{\text{active}}}{A_{\text{slab}}}. \tag{21}$$

The maximum extractable energy, $E_{\text{extr}}$, for a zig-zag optical path is given as

$$E_{\text{extractable}} = E_{\text{avail}} f(2 - f). \tag{22}$$

The unextracted energy, $E_{\text{unextracted}}$, in the active area due to the zig-zag optical path is given by [48]

$$E_{\text{unextracted}} = E_{\text{avail}}(1 - f)^2. \tag{23}$$

Using Eqs. (6) to (23), the Yb:YAG MOPA system has been modeled to achieve 1 J of output energy with 100 nJ of input energy and 11.5 J of pump pulse energy. This is accomplished in four stages. The first two preamplifier stages, which utilize end-pumped slabs, can be used to scale to the 5 mJ level. Details of the final two power amplifier stages are presented in Section 4. In this section, we present the design and modeled performance of an end-pumped slab preamplifier. In Section 3, we present results of the experimental verification of this slab design.

### B. Design

The first step is to design a high-gain, ($G = E_{\text{out}}/E_{\text{in}}$), Yb:YAG end-pumped preamplifier. An efficient, high-gain preamplifier slab must have the following four properties. First, it must enable near total pump coupling, confinement, and absorption. The achieved $g_0 l_{\text{eff}}$ must not be limited by inadequate pump absorption. The second objective is to suppress parasitic oscillations at high peak pump powers and achieve an ASE-limited $g_0 l_{\text{eff}}$. Third, the signal must have minimal passive propagation losses and distortion across the beam wavefront. Fourth, a stress fracture must be avoided at the required average pump power.

Achieving all four goals in a slab requires a considerable amount of design iterations. This is because, typically, optimizing the parameters to achieve one objective makes achieving the others more difficult. The next few paragraphs describe the choices for some of the parameters.

The gain coefficient, $g_0$, is a function of the dynamic absorption and emission cross sections ($\sigma_{\text{dyn}}^{p}$ and $\sigma_{\text{dyn}}^{e}$), the upper-state lifetime ($\tau$), crystal properties ($w$ and $t$), input pump power ($P_{\text{pump}}^{pk}$, $\Delta t_{\text{pump}}$), and the dopant ion density ($n_d$). The dopant ion density is given by $n_d = D_p D_a$, where $D_p$ is defined as the atomic percentage doping of $Yb^{3+}$ ions, and $D_a$ is the $Yb^{3+}$ ion density per atomic percentage doping. The choice of the Yb:YAG gain material and operating temperature fixes $\sigma_{\text{dyn}}^{a}$, $\sigma_{\text{dyn}}^{e}$, $\tau$, $D_a$, and $F_{\text{sat}}$. The remaining free parameters relating to the crystal (i.e., $w$, $t$, $l_{\text{doped}}$, $l_{\text{undoped}}$, $D_p$, $\alpha$), the input signal (i.e., $w_g$, $\theta_1$), and the pump power (i.e., $P_{\text{pump}}^{pk}$, $\Delta t_{\text{pump}}$) are selected to achieve the maximum parasitic-limited $g_0 l_{\text{eff}}$ and maximize $E_{\text{stored}}$.

One of the first constraints in amplifier design is the highly multimode nature of the diode-laser pump sources. At the time this project was initiated, 250 W, 0.22 NA, 600 μm core fiber-coupled diode pump lasers were commercially available. When this fiber output is focused to a 400 μm spot size, the NA increases to approximately 0.37. Because of the large pump divergence angle the slab must guide the pump light by TIR along the slab absorption length.

Substituting Eq. (16) into Eq. (12) shows that the slab amplifier's $g_0 l_{\text{eff}}$ is proportional to the pump intensity, $I_{\text{in}}(t)$, and consequently also proportional to $\eta_{p-\text{loss}}(P_{\text{pump}}^{pk}/A_{\text{slab}})$. Using $w$, $l$, $t$, $D_p$, and $P_{\text{pump}}^{pk}$ as free parameters, Eq. (12) is numerically solved to yield the small signal logarithmic gain of a slab amplifier.

Figure 3 shows a plot of the calculated logarithmic gain as a function of $D_p l_{\text{eff}}$. For small $D_p l_{\text{eff}}$, increasing the doping or the length increases the logarithmic gain because of increased pump absorption. For large $D_p l_{\text{eff}}$, increasing the doping or the length reduces the logarithmic gain because some parts of the doped region are not yet transparent at a given pump power, leading to absorption of the signal. As a result, there is an optimum $D_p l_{\text{eff}}$ that maximizes the gain. As the pump power is increased, the gain is maximized for longer absorption lengths. For $P_{\text{pump}}^{pk} = 120$ W, $w = t = 400$ μm, maximum $g_0 l_{\text{eff}} = 3$ is achieved for $D_p l_{\text{eff}}$ between 4 and 5. We chose to de-

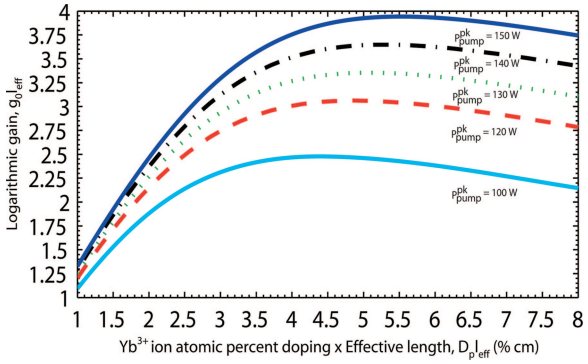


Fig. 3. (Color online) Calculated logarithmic gain, $g_0 l_{\mathrm{eff}}$, versus the atomic percent doping–length product $D_p l_{\mathrm{eff}}$. The peak incident pump power, $P_{\mathrm{pump}}{}^{pk}$, is the free parameter. The slab dimensions, $w = t = 400$ μm, and pump loss efficiency, $\eta_{p-\mathrm{loss}} = 1$, are assumed.

sign the slab with $D_p l_{\mathrm{eff}} = 4.57$. By using the relation $l_{\mathrm{eff}} = l_{\mathrm{doped}}/\cos\gamma$ and choosing a typical value of $\gamma \approx 29°$, we find that $D_p l_{\mathrm{doped}} = 4.32$. To avoid possible problems with nonradiative decay mechanisms in >5% doped Yb:YAG [33], we chose $D_p = 3\%$. The length of the doped region is thus given as $l_{\mathrm{doped}} = 1.44$ cm.

By reducing $A_{\mathrm{slab}}$, it is possible to achieve $g_0 l_{\mathrm{eff}} = 3$ at lower pump power levels. However, reducing $A_{\mathrm{slab}}$ would make the slab more difficult to fabricate. The $\mathrm{TEM}_{00}$ spot size of the signal, $w_g$, would also be required to be considerably smaller than 100 μm to minimize clipping losses. The length of each undoped end cap, $l_{\mathrm{undoped}}$, and bounce angle $\gamma$ are chosen to allow an integer number of bounces in the slab and further minimize propagation losses. In accordance with St. Venant's principle, we ensure that $l_{\mathrm{undoped}} > t$ to minimize thermal stresses. $\gamma$ is a function of the signal input angle at the end face, $\theta_1$, the slab tip angle, $\alpha$, and the index of refraction of YAG. The slab tip angle is fixed at 50° because simulations have shown that the parasitic oscillations are minimized [70]. $\theta_1$, $\gamma$, and $l_{\mathrm{undoped}}$ are iterated until the signal enters and exits the slab without clipping at the input and output end faces.

One final point regarding the slab dimensions concerns the choice of $w$ and $t$. The slab is designed to have a 1:1 [width (w)/thickness (t)] aspect ratio with $w \times t = A_{\mathrm{slab}}$. This aspect ratio enables easier operation with a $\mathrm{TEM}_{00}$ Gaussian beam in a multipass amplifier. A 1:1 (width/thickness) aspect ratio slab, first modeled by Kane *et al.* [42], also has the largest length to thickness aspect ratio. This minimizes the transverse ASE gain and maximizes the gain for the signal along the slab's length. Figure 4(a) depicts the slab dimensions in detail.

Suppression of parasitic oscillations is also a key goal that influences slab design, and in particular, the choice of coatings. This is because a parasitic oscillation is basically a laser with a threshold dependent on optical path losses. The simplest parasitic oscillation occurs when the slab itself forms the cavity. The threshold for parasitic oscillation is obtained

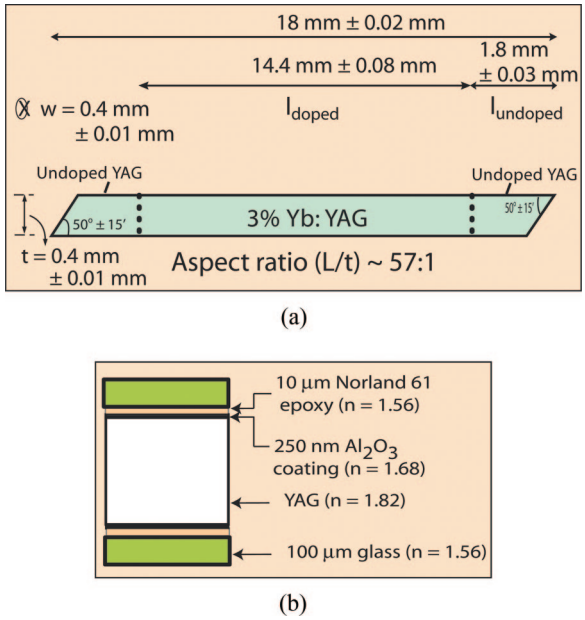


Fig. 4. (Color online) (a) Two-dimensional view of slab with dimensions and coating properties. The top and bottom are the TIR surfaces. They have a 250 nm $Al_2O_3$ AR coating that results in a power reflectivity of <2% for $\theta < 50°$ at 940 and 1030 nm. This layer is followed by a 10 μm layer of Norland 61 fluid and a 100 μm thick glass piece, which both have an index of 1.56. The two end faces have an AR coating at 940 and 1030 nm. At 940 nm the power reflectivity is <2% for $18° < \theta < 61°$. At 1030 nm the power reflectivity is <1% for $20° < \theta < 30°$. (b) End view of the slab with a description of the coating and cladding on the TIR faces.

by setting the gain equal to loss:

$$(g_0)_{\mathrm{parasitic}} = -\frac{1}{l_t}\ln\left(\prod_{i=1}^{N} R_i\right), \tag{24}$$

where $R_i$ is the parasitic loop's $i_{th}$ reflection coefficient, $l_T$ is the parasitic loop's total path length [71]. To maximize $(g_0)_{\mathrm{parasitic}}$, the reflection coefficient from each slab surface should be minimized and efforts should be taken to avoid closed loop optical paths that lower $(g_0)_{\mathrm{parasitic}}$. Several techniques have been investigated to minimize the reflection coefficient from the slab surfaces and suppress parasitic oscillations [44,71]. Absorbing edge claddings on disks have also been developed to absorb ASE and suppress parasitic oscillations [72]. This technique is now implemented in Nd:glass amplifier slabs at the National Ignition Facility at LLNL.

We recently presented enhanced parasitic oscillation suppression in Nd:YAG slab amplifiers using largely nonabsorptive claddings on the edge surfaces [45]. Those claddings are implemented here in Yb:YAG slabs. The cladding consists of an optical grade epoxy and a 100 μm thick piece of glass. The epoxy bonds the glass piece to YAG. The index of refraction of the cladding, $n_{\mathrm{clad}}$, is selected to transmit the parasitic modes incident on the side faces at $\theta < \theta_{\mathrm{crit}}$ while trapping the pump and signal rays that are incident on the faces at $\theta > \theta_{\mathrm{crit}}$. For a given slab width and

thickness, and divergence angle for the pump beam, we calculate the minimum angle, $\theta_{min}$, at which pump rays are incident on the side faces. $\theta_{crit}$ is set just below this value so that all the pump rays are confined due to TIR and absorbed in the doped region. We chose a cladding material such that

$$\theta_{crit} \cong \sin^{-1}\left(\frac{n_{clad}}{n_{YAG}}\right). \quad (25)$$

For our experimental conditions, we chose $\theta_{crit} = 59°$ and used an optical-grade epoxy (Norland 61) with a refractive index of 1.56 as the cladding. To ensure that ASE rays in the cladding do not re-enter the slab through TIR at the cladding–air interface, the glass's interface with air is roughened to enable outward scattering.

The caption in Fig. 4(a) lists the properties of the coatings on the slab's end and TIR surfaces. Figure 4(b) is an end view of the slab. The slab is conduction cooled on the top and bottom faces. First, a 250 nm $Al_2O_3$ ($n = 1.68$) coating is placed on the slab to reduce reflections of the ASE from the cladding that follows. A 10 μm thick Norland 61 ($n = 1.56$) optical-grade epoxy deposited on these surfaces assures TIR zig-zag reflections for the signal beam with minimum loss by allowing the evanescent wave to be attenuated. The bounce angle for the signal beam, $\gamma$, is chosen such that $\pi/2 - \gamma > \theta_{crit}$. The net loss for the signal beam due to residual scattering at the YAG–$Al_2O_3$–Norland interface is less than 0.1% per bounce. Because the Norland 61 layer is somewhat nonuniform in thickness and difficult to roughen for parasitic suppression, we place a 100 μm thick Schott Glass ($n = 1.56$) on top of the Norland 61 layer. The Norland 61 fluid is the glue that binds the Schott glass layer and YAG. A 125 μm thin indium foil thermal layer followed by copper coolers are placed in contact with the 100 μm thick glass plate to extract the heat deposited under operating conditions in the slab.

In our implementation, the 250 nm $Al_2O_3$ coating provides improved optical performance. It suppresses parasitic oscillations by increasing the loss for SE or ASE rays that are incident on the TIR surfaces at less than the critical angle ($\theta_{crit}$). This coating has a less than 2% power reflectivity for ASE rays that are incident on the TIR surfaces from within the slab at angles less than approximately $0.9 \times \theta_{crit}$; $\theta_{crit}$ for a YAG–$Al_2O_3$–Norland 61 interface is 59°, whereas for a YAG–air interface it is 33.2°. The coating allows more ASE rays to refract out of the slab and into the Norland 61 layer and eventually be scattered at the glass–air interface or absorbed in the indium thermal layer or copper cooler that is in contact with the glass.

An AR coating is also deposited on each of the end-coupling faces of the slab. This coating is a multilayer AR coating at $\lambda_p$ and $\lambda_s$. The coating enables efficient pumping of slabs and ensures minimal loss to the amplified signal beam. By reducing the reflectivity for the ASE as well, the AR coating at $\lambda_s$ also increases the parasitic oscillation threshold. The edge faces are polished at the end of fabrication to help contain the pump radiation via TIR.

Fabrication of a high length to thickness aspect ratio slab (0.4 mm × 0.4 mm × 18 mm, doped region with undoped end caps) presents challenges. Slabs fabricated individually are of lower quality (surface flatness and coating properties are not uniform), and higher cost (10 times higher) than slabs made by the batch fabrication process. We therefore developed a mass fabrication technique that produced multiple slabs but involved intermediate polishing and coating steps that utilized large surface areas [73]. The steps include bonding undoped YAG to either side of a doped YAG block to form a sandwich, and dicing the sandwich to provide slices. Two of the surfaces of each slice are cut, ground, and polished as TIR surfaces. The slice's end surfaces and the TIR surfaces are appropriately coated. The coated slice is then diced perpendicular to the TIR surfaces and the edges are polished to provide many zig-zag slabs. Finally, a 100 μm glass plate is glued to the slab's TIR faces with a Norland 61 optical-grade epoxy.

### C. Model Performance

The expected performance of the Yb:YAG preamplifier is modeled using Eqs. (6)–(8). The model accounts for spontaneous emission losses but does not include ASE or parasitic oscillations. The initial goal is to determine the peak incident pump power required to achieve $g_0 l_{eff} > 3$. Figure 5 shows the modeled $g_0 l_{eff}$ versus $P_{pump}^{pk}$ of a slab preamplifier whose properties are given in Fig. 4(a). For these values, the model predicts $g_0 l_{eff} = 3$ at 120 W of peak incident pump power. We also modeled the logarithmic gain as a function of pump pulse duration, $\Delta t_{pump}$. This can be used to study the trade-off between peak pump power and pump pulse duration for a desired value of logarithmic gain, $g_0 l_{eff}$. In situations where the available peak pump power is limited, it may be possible to achieve the desired $g_0 l_{eff}$ value by using longer pump pulses. The increased thermal load on the crystal needs to be managed in such cases. Calculations

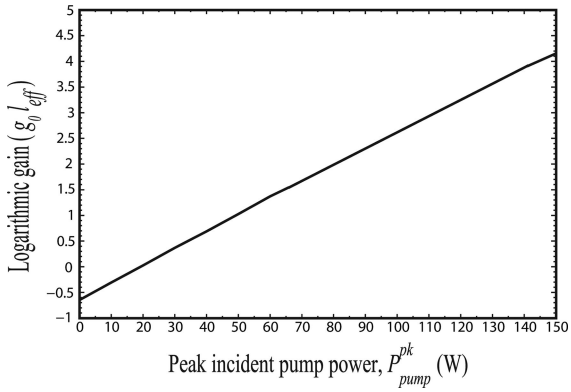


Fig. 5. Modeled amplifier small signal logarithmic gain, $g_0 l_{eff}$ versus incident pump power, $P_{pump}^{pk}$ (W). Here we assume a pump loss efficiency, $\eta_{p-loss} = 0.9$, $\gamma = 29°$, $A_{slab} = 0.16\ mm^2$, $\sigma_{dyn}^{e} = 2.1 \times 10^{-20}\ cm^2$.

show that $g_0 l_{\text{eff}}$ increases rapidly up to 75% of its maximum value for $\Delta t_{\text{pump}} \simeq \tau$, and increases much more slowly thereafter. Recall that the upper-state lifetime, $\tau$, of Yb:YAG is 0.951 ms. At 120 W of peak incident pump power, $g_0 l_{\text{eff}} \approx 3$ is achieved by pumping for $\Delta t_{\text{pump}} = 1$ ms.

### 3. Amplifier Performance

Figure 6 shows the experimental setup for the single-pass Yb:YAG slab preamplifier measurements. Fiber-coupled laser diodes at 940 nm from Apollo Instruments are used to pump the slab's right end. The diode is electrically modulated to produce nearly top-hat 1 ms optical pulses at 10 Hz with up to 150 W of peak power.

The 1.030 μm probe beam to measure the amplifier gain comes from a 100 mW cw fiber laser that is externally modulated to produce 1 μs pulses at 10 Hz. The signal pulses arrive at the slab from the left at the end of the pump pulse. They are focused to $w_g = 100$ μm at the slab's input face.

#### A. Slab with Cladding on Total Internal Reflection Faces

Figure 7 shows the experimentally measured logarithmic gain versus peak incident pump power for the fabricated slab with polished edges and parasitic suppression on only the TIR faces. Due to parasitic oscillations, the $g_0 l_{\text{eff}}$ of this slab amplifier is pinned at 1.2 at 135 W of pump power. Visual inspection of the polished side faces of the slab under pumping conditions confirms that the pump confinement is nearly 100%. The slab with all sides polished provides high reflectivity from the surfaces and permits parasitic oscillations to clamp the gain. Since the extracted power in a saturated amplifier is proportional to $g_0 l_{\text{eff}}$, this amplifier slab is unsuitable for efficient amplification. Next, we focus on ways to increase the gain of the fabricated slab.

#### B. Slab with Cladding on Face and Edge Faces

To achieve enhanced parasitic suppression, the slab is modified to have claddings on the edge and TIR (side) faces. Figure 7 also shows the experimental measured and theoretical logarithmic gain ($g_0 l_{\text{eff}}$) versus peak incident pump power $P_{\text{pump}}^{pk}$(W) for this slab. The logarithmic gain reaches three at a pump power of 137 W. We use $\eta_{p-\text{loss}}$ as a fitted parameter, and by setting $\eta_{p-\text{loss}} = 0.9$ in Eq. (16), the theoretical and experimental curves match quite well. Ten percent of pump light is lost due to inadequate coupling (mode matching + AR coating losses) or not confined due to TIR in the slab. The single-pass transmission of a low power 1.064 μm beam through the slab was measured to be 98%. This corresponds to approximately 0.1% per bounce of passive loss.

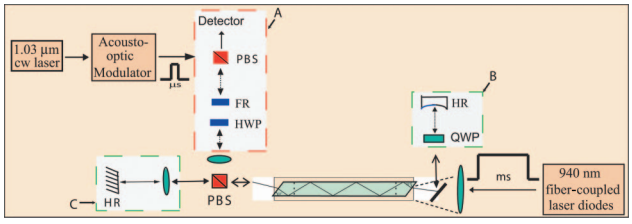


Fig. 6. (Color online) Schematic of quadruple-pass slab amplifier experiment setup. The optical elements in boxes A, B, and C need to be removed to make a single-pass gain measurement. In this case, the detector is placed at the location of box B. For a double-pass gain measurement, the elements in boxes A and C are not required. The detector is placed at the location of box C for this gain measurement. The abbreviations HR, QWP, HWP, FR, and PBS, stand for high reflector, quarter-wave plate, half-wave plate, Faraday rotator, and polarizing beam splitter, respectively.

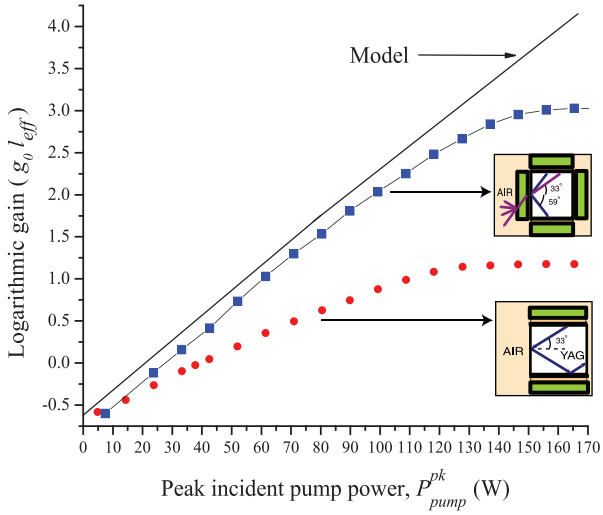


Fig. 7. (Color online) Parasitic-limited logarithmic gain, $g_0 l_{\text{eff}}$, versus pump power, $P_{\text{pump}}^{pk}$ (W), is shown. The solid line represents the gain that would be expected from theory using Eq. (12). Here, $\eta_{p-\text{loss}} = 0.9$ is assumed in the model. The dots are experimental measured gain values achieved using the setup shown in Fig. 6. The plotted dot values are derived by using Eq. (7) and calculating $\ln[E_{\text{out}}/(\eta_{s-\text{loss}} \cdot E_{\text{in}})]$ for measured values of $E_{\text{out}}$ and $E_{\text{in}}$ and assuming signal loss efficiency, $\eta_{s-\text{loss}} = 1$. The inset shows the end view of a slab with parasitic suppression only on the TIR faces (dots show corresponding gain) as well as a slab with claddings on edges of the slab for parasitic suppression (squares show corresponding gain).

We also measured the logarithmic gain versus pump pulse duration, $\Delta t_{\text{pump}}$. There is marginal benefit to the gain for pumping at intervals longer than $\tau$. At 137 W of peak incident pump power, the parasitic-limited $g_0 l_{\text{eff}} \approx 3$ is achieved for $\Delta t_{\text{pump}} = 1$ ms. Model calculations predict that at 120 W of peak incident pump power, a $g_0 l_{\text{eff}} \approx 3$ is achieved by pumping for $\Delta t_{\text{pump}} = 1$ ms. By accounting for additional pump loss and setting $\eta_{p-\text{loss}} = 0.9$, the measured and modeled values agree to within 3%. Uncertainty in $\eta_{s-\text{loss}}$ and measurements of $P_{\text{pump}}^{pk}$ could explain the small discrepancy between the model and experiment. Pumping at peak powers greater than 137 W results in a parasitic-limited $g_0 l_{\text{eff}} = 3$ at shorter pump pulse durations.

The first fabricated slab with parasitic suppression only on the TIR faces showed parasitic limited unsaturated logarithmic gain, $g_0 l_{\text{eff}} = 1.2$. To achieve higher gains parasitic suppression claddings were added to the edge faces as well. The parasitic limited

logarithmic gain is increased by nearly a factor of 2.4 with edge claddings. Furthermore, the resulting $g_0 l_{\text{eff}} = 3$, is close to the ASE-limited logarithmic gain, which is expected to be between 3 and 4.

Operating at the parasitic-oscillation-pinned logarithmic gain has the side benefit that the pump power can be increased to keep the gain constant against fluctuations in gain due to laser diode pump power fluctuations. The stored energy density in this slab amplifier is 15.6 J/cm$^3$. The significantly enhanced small signal gain in the slab with claddings on the non-TIR (edge) faces offers the potential for increased pulse energy extraction in a saturated MOPA configuration.

### C. Multipass Amplifier Performance

The slabs with parasitic suppression claddings on all four sides demonstrate the best logarithmic gain performance. These slab amplifiers were tested in a multipass amplifier configuration. This yields an estimate of the maximum possible gain in an Yb:YAG slab amplifier. At the time these tests were performed, the end face of the slab was slightly chipped due to pump light partially missing the slab during alignment. As a consequence, the pump light incoupling efficiency was reduced and additional pump light was required to achieve the parasitic limited gain.

We set up an experiment to quadruple pass the slab amplifier. Figure 6 illustrates the details of the experiment. First, double pass of the amplifier is accomplished by reimaging the output of the first pass back into the slab with an appropriately chosen curved mirror. The polarization of the beam during the second pass is rotated by 90° to allow separation of the output with a polarization beam splitter.

The double-pass amplifier enables a net $g_0 l_{\text{eff}}$ of 5 at $P_{\text{pump}}{}^{pk} = 250$ W before clamping due to parasitic oscillations. The fact that the gain is less than $e^6$ suggests additional losses on the return path and imperfect reimaging. The beam quality of the double-passed output radiation was also measured. $M^2$ is determined to be 1.23 in the $x$ direction and 1.08 in the $y$ direction.

To accomplish quadruple passes of the amplifier, the output after the second pass is reimaged back onto the slab. After the fourth pass, the half-wave plate and Faraday rotator effectively rotate the polarization of the beam by 90° and allow separation of the input beam and quadruple-pass output with an additional polarization beam splitter.

Figure 8 shows that the quadruple-pass slab amplifier enables a net small-signal gain of $e^8$ before clamping due to parasitic oscillations. The fact that the small signal gain is less than $e^{12}$ suggests imperfect reimaging and additional clipping losses. The beam quality of the quadruple-pass output radiation could not be measured because of technical difficulties.

The quadruple pass amplifier experiment described above was operated in the unsaturated regime due to limited available input signal energy.

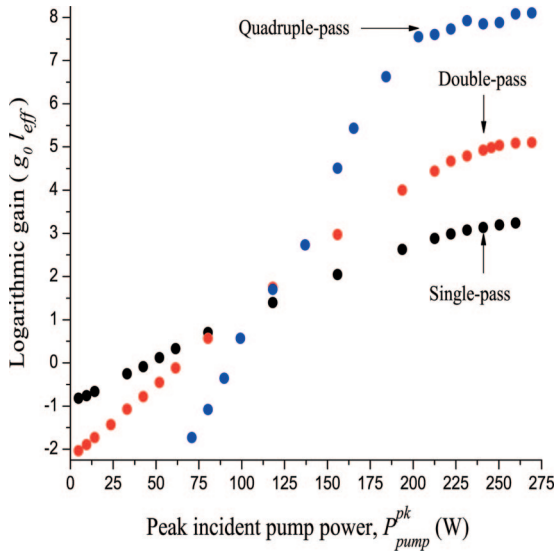


Fig. 8. (Color online) Logarithmic gain, $g_0 l_{\text{eff}}$, versus peak incident pump power, $P_{\text{pump}}{}^{pk}$ (W), for a single-, double-, and quadruple-pass end-pumped slab amplifier with edge claddings for parasitic suppression.

The 100 mW cw master oscillator modulated into microsecond pulses produces 25 nJ/μs pulses at the slab's input face due to the diffraction efficiency and propagation losses of the acousto-optic modulator (AOM). After the quadruple pass the output pulse energy is approximately 72 μJ. The alignment of the quadruple-pass amplifier was extremely sensitive to mirror positions. Small amounts of intentional misalignment resulted in parasitic oscillation. The slab amplifier is much less likely to break into parasitic oscillation in the double-pass configuration and is therefore more stable.

To saturate the double-pass slab amplifier, approximately 100 μJ of input pulse energy is required. Preamplification of the AOM output in a 30 μm core diameter fiber conservatively will allow generation of 5–10 μJ pulses in a good spatial mode. Model calculations suggest that 100 μJ/μs may be generated with available input signal energy. These developments will allow saturation of the double-pass, end-pumped, slab amplifier and yield 5 mJ/μs pulses. This output can then be used to seed the two-slab power amplifier to reach the 1 J level. This is modeled in Section 4.

## 4. Design of Two-Slab Power Amplifier

For space-based wind velocity measurements, we estimate that 1 J 1.03 μm pulses are required to generate 150 mJ at 1.55 μm by optical parametric amplification. The experimental accomplishments described in this paper form the basis for scaling the Yb:YAG MOPA to the 1 J level. The demonstrated single-pass parasitic-limited logarithmic gain, $g_0 l_{\text{eff}}$, is 3 at 137 W of peak incident pump power. The gain volume of the preamplifier slab is $2.3 \times 10^{-3}$ cm$^3$. The stored energy is ≈36 mJ and the stored energy density in the preamplifier slab is 15.6 J/cm$^3$. The

Table 1. End-Pumped Yb:YAG Slab Power Amplifier Physical Properties

| | Brief Description | Units | 100 mJ Slab | 1 J Slab |
|---|---|---|---|---|
| 1 | Total crystal length, $l$ | mm | 19.8 | 50 |
| 2 | Total doped crystal length, $l_{\text{doped}}$ | mm | 16.6 | 36.6 |
| 3 | Undoped crystal length on each end, $l_{\text{undoped}}$ | mm | 1.6 | 6.7 |
| 4 | Crystal width, $w$ | mm | 1.1 | 3.5 |
| 5 | Crystal thickness, $t$ | mm | 1.1 | 3.5 |
| 6 | Apex angle on both ends, $\alpha$ | deg | 50 | 50 |
| 7 | $Yb^{3+}$ atomic doping concentration | % | 3 | 1.3 |
| 8 | Zig-zag slab bounce angle for first pass, $\gamma_1$ | deg | 24.93 | 24.04 |
| 9 | Zig-zag slab bounce angle for second pass, $\gamma_2$ | deg | 30.15 | 30.75 |
| 10 | Number of zig-zag bounces on first pass | | 8 | 6 |
| 11 | Number of zig-zag bounces on angular-multiplexed, second pass | | 10 | 8 |

double-pass Yb:YAG end-pumped preamplifier can be operated in saturation to generate approximately 3.5–5 mJ/μs pulses. The goal of this section is to use these results and model a two-slab power amplifier to generate 1 J pulses.

The design will also draw upon the lessons learned from the cw Nd:YAG saturated amplifiers recently demonstrated in our lab [45]. Those results show that a saturated, end-pumped, zig-zag slab amplifier has a net active-area amplifier extraction efficiency of 80% with excellent beam quality ($M^2 < 1.1$). The amplifier was operated in a double-pass configuration with angular multiplexing [74] on the second pass to extract power from slab regions that were not probed during the first pass. This experimental result is used as a benchmark for the Yb:YAG power amplifier model because the analytic theory for an angle-multiplexed, double-passed, saturated zig-zag slab amplifier does not exist. The single-pass Yb:YAG power amplifier output is modeled using Eqs. (6)–(23), and the double-pass output is predicted using the Nd:YAG MOPA experimental benchmark.

### A. Design of 100 mJ End-Pumped Slab Amplifier

Tables 1 and 2 summarize the characteristics of the slabs required for scaling to the 100 mJ level and then further to the 1 J level. The slab is designed to have claddings on the edges as well as the TIR faces for parasitic suppression.

Table 1 lists the dimensions of the composite slab amplifier. The parameters are derived by using Eqs. (6)–(23) and following the procedure described in Subsection 2.B. For scaling to the 100 mJ level, the slab's width to thickness aspect ratio is 1:1 and the doped length to thickness aspect ratio is 16:1. The percent doping and effective length product is five, chosen to maximize the gain for the chosen input pump power and slab cross-section area.

Table 2 shows the calculated input and output preamplifier performance properties. The 5 mJ input pulse is focused to a beam size, $w_g = 330$ μm in the slab. It undergoes eight bounces on the first pass and by entering the slab at a different angle, makes ten bounces on the return pass. On the second pass, the

Table 2. End-Pumped Slab Power Amplifier Input and Output Parameters

| | Brief Description | Units | 100 mJ Slab | 1 J Slab |
|---|---|---|---|---|
| 1 | Peak pump power | W | 1134 | 11,475 |
| 2 | Peak pump power pulse duration, $\Delta t_{\text{pump}}$ | ms | 1 | 1 |
| 3 | Pump and signal pulse repetition rate | Hz | 40 | 40 |
| 4 | Average pump power | W | 45.4 | 459 |
| 5 | Signal pulse duration | μs | 1 | 1 |
| 6 | 1030 nm signal input pulse energy, $E_{\text{in}}$ | mJ | 5 | 100 |
| 7 | Gaussian beam waist size, $w_g$ | mm | 0.33 | 1.1 |
| 8 | Logarithmic gain, $g_0 l_{\text{eff}}$ | | 3 | 3 |
| 9 | Stored energy, $E_{\text{stored}}$ | J | 0.277 | 2.8 |
| 10 | Active area available energy, $E_{\text{avail}}$ | J | 0.121 | 1.24 |
| 11 | Zig-zag path extractable energy, $E_{\text{extractable}}$ | J | 0.050 | 0.55 |
| 12 | Single-pass output energy, $E_{\text{out}}$ | J | 0.035 | 0.503 |
| 13 | Heat extraction fluence[a] | $W/cm^2$ | 12.4 | 17.9 |
| 14 | Preamplifier optical-to-optical efficiency ($\eta * 100$) | % | 8.7 | 8.7 |
| 15 | Predicted double-pass output energy | J | 0.1 | 1 |
| 16 | Average signal output power | W | 4 | 40 |

[a]Ten percent of the absorbed pump power is converted to heat.

signal extracts from regions that have not been probed during the first pass.

Table 2 also lists the performance parameters of the 100 mJ slab preamplifier. The 5 mJ input signal pulses are derived from a quadruple- or double-pass end-pumped zig-zag slab preamplifier. For a slab with properties listed in Table 1 and signal input parameters in Table 2, Eq. (6) predicts a 35 mJ output from the first pass. By using angular multiplexing on the second pass and increasing saturation, the output is predicted to be approximately 100 mJ/μs at 40 Hz. Eighty percent of the extractable energy in the active area of the slab is extracted and the heat extracted by conduction cooling is ≈12.4 W/cm$^2$; significantly below the stress fracture limit.

### B. Design of 1 J End-Pumped Slab Amplifier

Tables 1 and 2 summarize the design of a 1 J slab power amplifier as well. Table 1 lists the physical properties of the composite slab. The parameters are derived by using Eqs. (6) to (23) and following the procedure described in Subsection 2.B. The width to thickness aspect ratio is 1:1 and the doped length to thickness aspect ratio is 11:1. The $Yb^{3+}$ ion atomic percent doping and effective length product is 4.8, chosen to maximize the gain for the input pump power and slab cross-section area. The $Yb^{3+}$ ion at. % doping is reduced from 3 to 1.3 in the 1 J amplifier slab, and and the doped length is increased by the same factor to achieve a 11:1 doped length to thickness aspect ratio. We expect that this will mitigate the effects of transverse ASE and enable $g_0 l_{\text{eff}} = 3$ at 11.5 kW of peak pump power. Another consequence of these choices is that the stored energy density is effectively reduced to 6.24 J/cm$^3$ in this slab.

Table 2 lists the input and output optical properties of the slab amplifier. The 100 mJ input pulse is focused to a $w_g = 1.1$ mm in the slab. It undergoes six bounces on the first pass and by entering the slab at a different angle, makes eight bounces on the return pass. On the second pass, the signal extracts from regions that have not been probed during the first pass.

Table 2 also shows the expected performance parameters of the 1 J slab amplifier. For a slab with properties listed in Table 1 and signal input parameters in Table 2, Eq. (6) predicts a 503 mJ output from the first pass. By using angular multiplexing on the second pass and increased saturation, the output is predicted to be approximately 1 J/μs at 40 Hz. The total pump energy per pulse is 11.5 J. 70% of the extractable energy in the active area of the slab is extracted after the double pass and the heat extracted by conduction cooling is approximately 17.9 W/cm$^2$: significantly below the stress fracture limit.

The designed 1 J end-pumped Yb:YAG MOPA at 40 Hz requires 11.5 J of pump energy and will therefore operate at an optical-to-optical efficiency of 8.7%. The efficiency can be improved further by using spatially shaped super-Gaussian signal pulses that extract a greater fraction of the stored energy. Laser diodes currently operate at greater than 60% electrical efficiency and so we expect a laser system electrical efficiency of 5.1% at the 1.03 μm output wavelength.

The designed system operates at 40 Hz and 40 W of average output power at 1.03 μm. The average power scaling limit of the Yb:YAG end-pumped slab amplifiers needs to be determined. Greater than 200 W/cm$^2$ can be extracted from the slab directly contacted with the copper coolers with intermediate diamond heat spreaders. However, the slabs described here have claddings made of epoxy and glass. The stress fracture limit of the YAG–glass composite slab needs to be determined.

## 5. Conclusion

Based on the modeling and experimental measurements described earlier, we designed a 1 J Yb:YAG MOPA system as a step toward meeting the laser requirements for space-based remote wind sensing. Parasitic oscillations are key limitations to energy storage and efficient energy extraction. We investigated different methods of parasitic oscillation suppression to improve energy storage. Slabs with a cladding on just the TIR faces have a maximum $g_0 l_{\text{eff}}$ of 1.2. We improved this result by incorporating a novel technique involving claddings on the edge faces. Using this technique, a maximum $g_0 l_{\text{eff}}$ of 3 is achieved at 137 W of pump power. This represents a 250% improvement in the gain and energy storage of a single-pass, end-pumped, zig-zag slab amplifier. Further, the gain achieved is close to the limit posed by ASE. The significant improvements in slab amplifier performance using claddings for parasitic suppression are made possible by an accompanying development in the slab fabrication technique. The batch fabrication technique improves the quality and dramatically reduces the complexity and cost of producing zig-zag slabs. This advance allowed us to evaluate the effectiveness of various parasitic suppression techniques in a time and cost-effective way. The combination of parasitic suppression and batch fabrication may enable significantly increased utility of zig-zag slabs in high-power, solid-state laser and amplifier systems.

The designed 1 J end-pumped Yb:YAG MOPA at 40 Hz will operate at an optical-to-optical efficiency of 8.7%. Laser diodes currently operate at greater than 60% efficiency so that we may expect a laser system electrical efficiency of 5.1% at the 1.03 μm output wavelength. This system can be used to pump parametric amplifiers at 1.55 μm for eye-safe wind sensing from a space platform.

Finally, the future of laser transmitters for global wind measurements may go in a different direction. We are preparing a separate paper in which we reconsider the long-standing notion that eye-safe operation of a space-based wind lidar system is possible only at wavelengths greater than 1.4 μm. We show that it may be possible to achieve eye-safe operation

at 1 μm. Operating at this wavelength would make a space-based wind-sensing mission practical in the near future because of well-developed lidar subsystem technologies.

We thank the reviewers for their detailed and insightful comments. We also thank former students Todd Rutherford and William Tulloch, visiting scientist Ulrich Wittrock, and Michel Digonnet for useful discussions. Ted Judd from Crystal River Optics skillfully fabricated all the slabs. This work was supported in part by National Aeronautics and Space Administration grant NAS1-00104 and by the U.S. Army Research Office under grant DAAD19-02-1-0184.

## References

1. A. K. Sridharan, "Yb:YAG master oscillator power amplifier and PPLN optical parametric amplifiers for remote wind sensing," Ph.D. dissertation (Stanford University, 2007).
2. S. W. Henderson, R. M. Huffaker, M. J. Kavaya, C. P. Hale, J. R. Magee, and L. E. Myers, "Pulsed coherent solid-state 1.06 μm and 2.1 μm laser radar systems for remote velocity measurement," Proc. SPIE **1222,** 118–129 (1990).
3. S. W. Henderson, P. J. M. Suni, C. P. Hale, S. M. Hannon, J. R. Magee, D. L. Bruns, and E. H. Yuen, "Coherent laser radar at 2 μm using solid-state lasers," IEEE Trans. Geosci. Remote Sens. **31,** 4–15 (1993).
4. P. J. M. Suni, G. Gates, E. H. Yuen, D. L. Bruns, S. R. Vetorino, and T. J. Valle, "A diode-pumped 2 μm transceiver for ground and airborne doppler lidar measurements," in *Proceedings of the 7th Conference on Coherent Laser Radar Applications and Technology* (1993), pp. 206–209.
5. R. Targ, B. C. Steakley, J. G. Hawley, L. L. Ames, P. Forney, D. Swanson, R. Stone, R. G. Otto, V. Zarifis, P. Brockman, R. S. Calloway, S. H. Klein, and P. A. Robinson, "Coherent lidar airborne wind sensor II: flight test results at 2 and 10 μm," Appl. Opt. **35,** 7117–7127 (1996).
6. J. Yu, B. C. Trieu, E. A. Modlin, U. N. Singh, M. J. Kavaya, S. Chen, Y. Bai, P. J. Petzer, and M. Petros, "1 J/pulse *Q*-switched 2 μm solid state laser," Opt. Lett. **31,** 462–464 (2006).
7. V. Srivastava, J. Rothermal, A. D. Clarke, J. D. Spinhirne, R. T. Menzies, D. R. Cutten, M. A. Jarzembski, D. A. Bowdle, and E. M. McCaul, "Wavelength dependence of backscatter by use of aerosol microphysics lidar data sets: application to 2.1-μm wavelength for space-based and airborne lidars," Appl. Opt. **40,** 4759–4769 (2001).
8. S. M. Hannon and J. A. Thomson, "Aircraft wake vortex detection and measurement with pulsed solid-state coherent laser radar," J. Mod. Opt. **41,** 2175–2196 (1994).
9. S. W. Henderson, P. Gatt, D. Rees, and R. M. Huffaker, *Laser Remote Sensing* (CRC, 2005).
10. J. E. Midwinter, "The theory of *Q*-switching applied to slow switching and pulse shaping for solid state lasers," Br. J. Appl. Phys. **16,** 1125–1133 (1965).
11. E. Panarella and L. L. T. Bradley, "Controlled timewise redistribution of laser energy," IEEE J. Quantum Electron. **QE-11,** 181–184 (1975).
12. W. E. Schmid, "Pulse stretching in a *Q*-switched Nd:YAG laser," IEEE J. Quantum Electron. **QE-16,** 790–794 (1980).
13. J. Harrison, G. A. Rines, and P. F. Moulton, "Stable-relaxation-oscillation Nd lasers for long-pulse generation," IEEE J. Quantum Electron. **24,** 1181–1187 (1988).
14. J. P. Roberts, K. W. Hosack, A. J. Taylor, J. Weston, and R. N. Ettelbrick, "Efficient frequency-doubled long pulse generation with a Nd:Glass/Nd:YAG oscillator-amplifier," Opt. Lett. **18,** 429–431 (1993).
15. N. M. Wannop, M. R. Dickinson, A. Charlton, and T. A. King, "*Q*-switching the erbium-YAG laser," J. Mod. Opt. **41,** 2043–2053 (1994).
16. W. Viöl and J. Uhlenbusch, "Generation of $CO_2$ laser pulses by *Q*-switching and cavity dumping and their amplification by a microwave excited $CO_2$ laser," J. Phys. D **29,** 57–67 (1996).
17. W. Koechner, *Solid-State Laser Engineering,* Vol. 1 of Springer Series in Optical Sciences, 5th ed. (Springer-Verlag, 1999).
18. H. W. Bruesselbach, D. S. Sumida, R. A. Reeder, and R. W. Byren, "Low-heat high-power scaling using InGaAs-diode-pumped Yb:YAG lasers," IEEE J. Sel. Top. Quantum Electron. **3,** 105–116 (1997).
19. M. Munz and G. Haag, "Saturation of the gain in laser amplifiers by feedback of amplified spontaneous emission (ASE)," Z. Phys. B **50,** 79–86 (1983).
20. D. Lowenthal and J. M. Eggleston, "ASE effects in small aspect ratio laser oscillators and amplifiers with nonsaturable absorption," IEEE J. Quantum Electron. **QE-22,** 1165–1173 (1986).
21. Q. Lü and S. Dong, "Numerical and experimental investigation on ASE effects in high-power slab amplifiers," Opt. Laser Technol. **25,** 309–314 (1993).
22. T. J. Kane and R. L. Byer, "62-dB gain multiple-pass slab geometry Nd:YAG amplifier," Opt. Lett. **11,** 216–219 (1986).
23. M. G. Knights, M. D. Thomas, E. P. Chicklis, G. A. Rines, and W. Seka, "Very high gain Nd:YLF amplifiers," IEEE J. Quantum Electron. **24,** 712–715 (1988).
24. G. H. Miller, E. I. Moses, and C. R. Wuest, "The National Ignition Facility," Opt. Eng. **43,** 2841–2853 (2004).
25. M. Shaw, W. Williams, R. House, and C. Haynam, "Laser performance operations model," Opt. Eng. **43,** 2885–2895 (2004).
26. M. L. Spaeth, K. R. Manes, C. C. Widmayer, W. H. Williams, P. K. Whitman, M. A. Henesian, I. F. Stowers, and J. Honig, "The National Ignition Facility wavefront requirements and optical architecture," Opt. Eng. **43,** 2854–2865 (2004).
27. L. F. Johnson, J. E. Geusic, and L. G. V. Uitert, "Coherent oscillations from $Tm^{3+}$, $Ho^{3+}$, $Yb^{3+}$, and $Er^{3+}$ ions in yttrium aluminum garnet," Appl. Phys. Lett. **7,** 127–129 (1965).
28. H. Bruesselbach and D. S. Sumida, "69-W-average-power Yb:YAG laser," Opt. Lett. **21,** 450–462 (1996).
29. L. D. DeLoach, S. A. Payne, L. L. Chase, L. L. Smith, W. L. Kway, and W. F. Krupke, "Evaluation of absorption and emission properties of $Yb^{3+}$ doped crystals for laser applications," IEEE J. Quantum Electron. **29,** 1179–1191 (1993).
30. P. Lacovara, H. K. Choi, C. A. Wang, R. L. Aggarwal, and T. Y. Fan, "Room-temperature diode-pumped Yb:YAG laser," Opt. Lett. **16,** 1069–1091 (1991).
31. T. Y. Fan, "Optimizing the efficiency and stored energy in quasi-three level lasers," IEEE J. Quantum Electron. **28,** 2692–2697 (1992).
32. P. Yang, P. Deng, and Z. Yin, "Concentration quenching in Yb:YAG," J. Lumin. **97,** 51–54 (2002).
33. M. Larionov, K. Schuhmann, J. Speiser, C. Stolzenburg, and A. Geisen, "Nonlinear decay of the excited state in Yb:YAG," in *Advanced Solid-State Photonics,* Technical Digest (Optical Society of America, 2005), paper TuB49.
34. L. M. Franz and J. S. Nodvik, "Theory of pulse propagation in a laser amplifier," J. Appl. Phys. **34,** 2346–2349 (1963).
35. R. M. Wood, *Laser-Induced Damage of Optical Materials* (Institute of Physics, 2002).
36. R. J. Beach, E. C. Honea, S. B. Sutton, C. M. Bibeau, J. A. Skidmore, M. A. Emanuel, S. A. Payne, P. V. Avizonis, R. S. Monroe, and D. G. Harris, "High-average-power pumped Yb:YAG lasers," Proc. SPIE **3889,** 246–260 (2000).
37. W. S. Martin and J. P. Chernoch, "Multiple internal reflection face pumped laser," U.S. patent 3,633,126 (4 January 1972).

38. W. B. Jones, "Face pumped laser with diffraction limited output beam," U.S. patent 4,214,216 (22 July 1980).
39. W. B. Jones, "Slab geometry laser," in *Handbook of Solid-State Lasers* (Marcel Dekker, 1989), pp. 581–612.
40. T. J. Kane, R. C. Eckardt, and R. L. Byer, "Reduced thermal focusing and birefringence in zig-zag slab geometry crystalline lasers," IEEE J. Quantum Electron. **QE-19,** 1351–1354 (1983).
41. J. M. Eggleston, T. J. Kane, K. Kuhn, J. Unternahrer, and R. L. Byer, "The slab geometry laser—Part I: theory," IEEE J. Quantum Electron. **QE-20,** 289–301 (1984).
42. T. J. Kane, J. M. Eggleston, and R. L. Byer, "The slab geometry laser—Part II: thermal effects in a finite slab," IEEE J. Quantum Electron. **QE-21,** 1195–1210 (1985).
43. R. J. Shine, Jr., A. J. Alfrey, and R. L. Byer, "40 W CW, $TEM_{00}$ mode, diode-laser-pumped, Nd:YAG miniature-slab laser," Opt. Lett. **20,** 459–462 (1995).
44. T. S. Rutherford, W. M. Tulloch, S. Sinha, and R. L. Byer, "Yb:YAG and Nd:YAG edge-pumped slab lasers," Opt. Lett. **26,** 986–989 (2001).
45. A. K. Sridharan, S. Saraf, S. Sinha, and R. L. Byer, "Zig-zag slabs for solid-state laser amplifiers: batch fabrication and parasitic oscillation suppression," Appl. Opt. **45,** 3340–3351 (2006).
46. A. D. Farinas, E. K. Gustafson, and R. L. Byer, "Design and characterization of a 5.5-W, cw, injection-locked fiber-coupled, laser-diode-pumped Nd:YAG miniature-slab laser," Opt. Lett. **19,** 114–117 (1994).
47. T. S. Rutherford, W. M. Tulloch, E. K. Gustafson, and R. L. Byer, "Edge-pumped quasi-three-level slab lasers: design and power scaling," IEEE J. Quantum Electron. **36,** 205–219 (1999).
48. J. M. Eggleston, L. M. Frantz, and H. Injeyan, "Derivation of the Frantz–Nodvik equation for zig-zag optical path, slab geometry laser amplifiers," IEEE J. Quantum Electron. **25,** 1855–1862 (1989).
49. R. J. S. Pierre, D. W. Mordaunt, H. Injeyan, J. G. Berg, R. C. Hilyard, M. E. Weber, M. G. Wickham, G. M. Harpole, and R. Senn, "Diode array pumped kilowatt laser," IEEE J. Sel. Top. Quantum Electron. **3,** 53–58 (1997).
50. G. D. Goodno, S. Palese, J. Harkenrider, and H. Injeyan, "High average-power Yb:YAG end-pumped zig-zag slab laser," in *Advanced Solid-State Lasers,* Vol. 50 of OSA Trends in Optics and Photonics Series, C. Marshall, ed. (Optical Society of America, 2001), pp. 2–4.
51. G. D. Goodno, H. Komine, S. J. McNaught, S. B. Weiss, S. Redmond, W. Long, R. Simpson, E. C. Cheung, D. Howland, P. Epp, M. Weber, M. McClellan, J. Sollee, and H. Injeyan, "Coherent combination of high-power, zigzag slab lasers," Opt. Lett. **31,** 1247–1249 (2006).
52. B. J. Comaskey, R. Beach, G. Albrecht, W. J. Benett, B. L. Freitas, C. Petty, D. VanLue, D. Mundinger, and R. W. Solarz, "High average power diode pumped slab laser," IEEE J. Quantum Electron. **28,** 992–996 (1992).
53. L. A. Hackel, R. J. Beach, C. B. Dane, and L. E. Zapata, "Laser driver for soft-x-ray projection lithography," Appl. Opt. **32,** 6914–6919 (1993).
54. M. J. Shoup III, J. H. Kelly, and D. L. Smith, "Design and testing of a large-aperture, high-gain, Brewster's angle zigzag Nd:glass slab amplifier," Appl. Opt. **36,** 5827–5838 (1997).
55. N. Hodgson, T. Haase, and H. Weber, "Improved resonator design for rod lasers and slab lasers," Proc. SPIE **1277,** 71–84 (1990).
56. N. Hodgson and T. Haase, "Beam parameters, mode structure and diffraction losses of slab lasers with unstable resonators," Opt. Quantum Electron. **24,** S903–S926 (1992).
57. N. Hodgson, S. Dong, and Q. Lu, "Performance of a 2.3-kW Nd:YAG slab laser system," Opt. Lett. **18,** 1727–1729 (1993).
58. Y. Chen, A. Rapaport, T. Y. Chung, B. Chen, and M. Bass, "Fluorescence losses from Yb:YAG slab lasers," Appl. Opt. **42,** 7157–7162 (2003).
59. Y. Chen, B. Chen, M. K. R. Patel, A. Kar, and M. Bass, "Calculation of thermal gradient induced stress birefringence in slab lasers—I," IEEE J. Quantum Electron. **40,** 909–916 (2004).
60. Y. Chen, B. Chen, M. K. R. Patel, A. Kar, and M. Bass, "Calculation of thermal gradient induced stress birefringence in slab lasers—II," IEEE J. Quantum Electron. **40,** 917–927 (2004).
61. T. Y. Chung and M. Bass, "General analysis of slab lasers using geometrical optics," Appl. Opt. **46,** 581–590 (2007).
62. A. Giesen, H. Hugel, A. Voss, K. Wittig, U. Brauch, and H. Opower, "Diode-pumped high-power solid-state laser: concept and first results with Yb:YAG," in *Advanced Solid-State Lasers,* T. Fan and B. Chai, eds., Vol. 20 of OSA Proceedings Series (Optical Society of America, 1994), paper YL2.
63. A. Giesen, H. Hügel, A. Voss, K. Wittig, U. Brauch, and H. Opower, "Scalable concept for diode pumped high power lasers," Appl. Phys. B **58,** 365–372 (1994).
64. A. Giesen, "High power thin disk lasers and applications," in *The 18th Annual Meeting of the IEEE Lasers and Electro-Optics Society, 2005* (IEEE, 2005), pp. 750–751.
65. C. Stewen, M. Larionov, A. Giesen, K. Contag, and H. Hügel, "A 1-kW CW thin disc laser," IEEE J. Sel. Top. Quantum Electron. **6,** 650–657 (2000).
66. H. E. Meissner and J. M. McMahon, "Composite solid state lasers of improved efficiency and beam quality," U.S. patent 5,563,899 (8 October 1996).
67. N. Traggis, Precision Photonics Corporation, Boulder, Colo. (personal communication, 2005).
68. A. E. Siegman, *Lasers* (University Science Books, 1987).
69. R. J. Beach, "Optimization of quasi-three level end-pumped *Q*-switched lasers," IEEE J. Quantum Electron. **31,** 1606–1613 (1995).
70. W. Long, Northrup Grumman Space Technology (personal communication, 2005).
71. D. C. Brown, D. P. Benfey, W. J. Gehm, D. H. Holmes, and K. K. Lee, "Parasitic oscillation and amplified spontaneous emission face-pumped total internal reflection lasers," Proc. SPIE **736,** 74–82 (1987).
72. H. T. Powell, "Composite polymer/glass edge cladding for Nova replacement disks," Tech. Rep. UCRL 50021-86 (Lawrence Livermore National Laboratory, 1986).
73. A. K. Sridharan, S. Saraf, and R. L. Byer, "Method for fabricating zig-zag slabs for solid state lasers," U.S. patent 7,087,447 (8 August 2006).
74. T. J. Kane, W. J. Kozlovsky, R. L. Byer, and C. E. Byvik, "Coherent laser radar at 1.06 μm using Nd:YAG lasers," Opt. Lett. **12,** 239–242 (1987).